REST Journal on Emerging trends in Modelling and Manufacturing
Vol:4(1),2018
REST Publisher
ISSN: 2455-4537

Website: www.restpublisher.com/journals/jemm

Synergistic effect between Sulphur dopant in $SrTiO_3$ lattice with surface sulphate species for enhancing visible light photo catalytic activity

B. G. Anitha, L. Gomathi Devi*
Department of Post Graduate Studies in Chemistry, Central College City Campus,
Dr. Ambedkar Street, Bangalore University, Bangalore 560001, India
Email: bganitha91@gmail.com and gomatidevi_naik@yahoo.co.in

Abstract

Sulphur was doped in to $SrTiO_3$ (STO) lattice by using sulphur powder as a sulphur source (S-STO). XPS results confirm the presence of S in two different oxidation states of S^{6+} and S^{2-}. PXRD results confirms the cubic perovskite structure for STO and S-STO. FTIR studies confirms the presence of surface sulphate species and PL studies implicates lower recombination rate for S-STO sample. UV-visible spectroscopic technique implicates the extended absorption in the visible region and lower band gap for S-STO. The higher oxidation state of S^{6+} compared to the host Ti^{4+} ion leads to the formation of various defects of the type V_o, $V_o^{\cdot}$, $V_o^{\cdot\cdot}$, V_{Ti}, to maintain the charge neutrality of the solid. These defects along with S^{6+} dopant and surface sulphate groups shows a synergistic effect in enhancing the photo catalytic activity of S-STO.

Keywords: Strontium titanate; Synergistic effect; photo degradation; hydroxyl radicals; X-ray photoemission spectroscopy.

1. Introduction

Strontium titanate ($SrTiO_3$) is one of the attractive semiconductor photo catalyst material for the photo catalytic degradation of environmentally hazardous pollutants in air and water under UV light illumination, due to its unique physical and chemical properties and other factors like high thermal stability, cost effective product which can be easily modulated to suit a particular reaction conditions and it is also found to be environmental friendly in nature (*1, 2*). However, the use of $SrTiO_3$ (STO) with an energy band gap of ~3.2 eV can be activated only under the UV light with wavelengths less than 388 nm. Many efforts have been made to extend its utilization under visible light. One such effort include incorporation of non-metal ions such as B, C, N, P, S and F to efficiently extend its photo response from the UV to the visible light region (*3, 4*). Non-metal ions are expected to get incorporated at oxygen lattice site narrowing the band gap of STO. The 2p orbitals of non-metal ions can create an acceptor level above the valence band (VB) if it occupies a substitutional lattice site or the 2p orbitals of non-metal ion and oxygen may get mixed up if the dopant occupy interstitial position. In addition non-metal ion doping can also induce certain cationic defects of the type Ti^{3+}, Ti^{3+}-V_o and anionic defects like neutral/charged oxygen vacancies to maintain the charge neutrality this in turn improve the visible light response of the STO (*5, 6*). In the past few years, many research groups have attempted to substitute many non-metal ions at the oxygen lattice site to modify the electronic properties and they have demonstrated that doping of such ions has improved the absorption characteristics of the catalyst especially under the visible light region (*7, 8*). In the present study we report the unique characteristics of S doped STO for the degradation of methyl violet as the model compound under solar light irradiation.

2. Results and discussion

2.1. PXRD studies

Fig.1shows the PXRD patterns of STO and S-STO samples. Both of STO and S-STO samples show the diffraction peaks at 2θ values of 22.70 (100), 32.35° (110), 39.91° (111), 46.42° (200), 57.72° (211), 67.74° (220) and 77.09° (310) which can be indexed to cubic pattern of STO (JCPDS card No: 74-1296). The numbers in the parenthesis represents hkl values. The average crystallite size was estimated based on line broadening of (110) peak for both STO and S-STO using the Scherer's Eq. (1).

$$D = \frac{k\lambda}{\beta \cos\theta} \qquad (1)$$

Where λ is the wavelength of Cu Kα source, β is full width at half maximum (FWHM) of (110) diffraction plane of $SrTiO_3$, k is a shape factor (0.94) and θ is angle of diffraction. The crystallite sizes are found to be 24.36 nm and 9 nm for STO and S-STO respectively. From the results it could be seen that incorporation of sulphur into the STO lattice inhibited the crystal growth (9). Lattice strain values were calculated from the following equation $\varepsilon = \beta/4\tan\theta$, where θ is the angle of diffraction and β is the FWHM (110) diffraction planes of STO and S-STO. The calculated lattice strain values were found to be 3.002×10^{-3} and 10×10^{-3} for STO and S-STO respectively. The higher lattice strain value and small shift in diffraction angle (110, 200 and 220 planes) towards higher value confirms the incorporation of S into STO lattice. The variation in lattice strain and

decrease in crystallite size, cell volume and lattice parameter of S-STO compared to STO further confirms the incorporation of S atoms in the STO matrix (Table. 1). The observed contraction in the cell volume of S-STO can attributed to the smaller ionic radius (0.029 nm) of incorporated S^{6+}dopant compared to the host Ti^{4+} ion (0.068 nm).

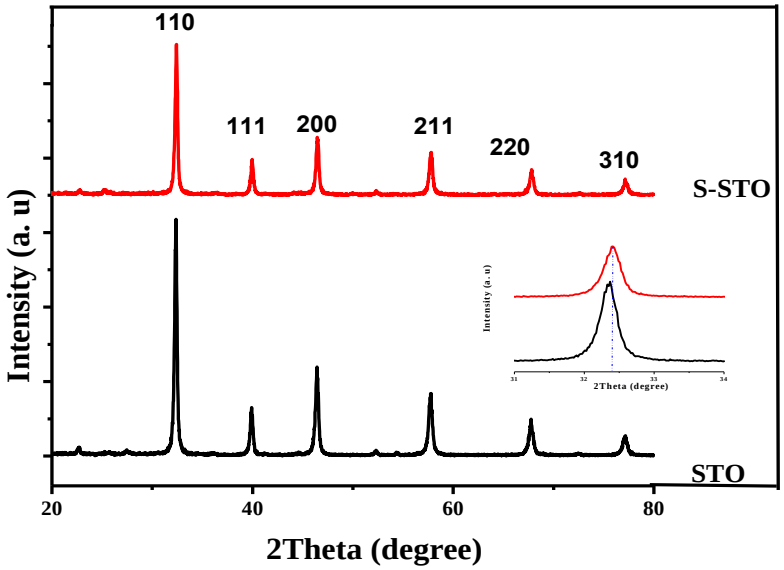

Fig.1. PXRD patterns of STO and S-STO samples.

Table 1. D= Crystallite size; A = lattice parameters in Å; V= Unit cell volume in $(Å)^3$ and Lattice strain ($\varepsilon \times 10^{-3}$) of STO and S-STO samples.

Samples	**D (nm)**	**A (A°)**	**V (A°)^3**	**$\varepsilon \times 10^{-3}$**
STO	24.36	a = b =c=3.9089	59.319	3.0023
S-STO	11.83	a = b =c=3.897	58.18	10.08

2.2. UV-Visible absorption spectral studies.

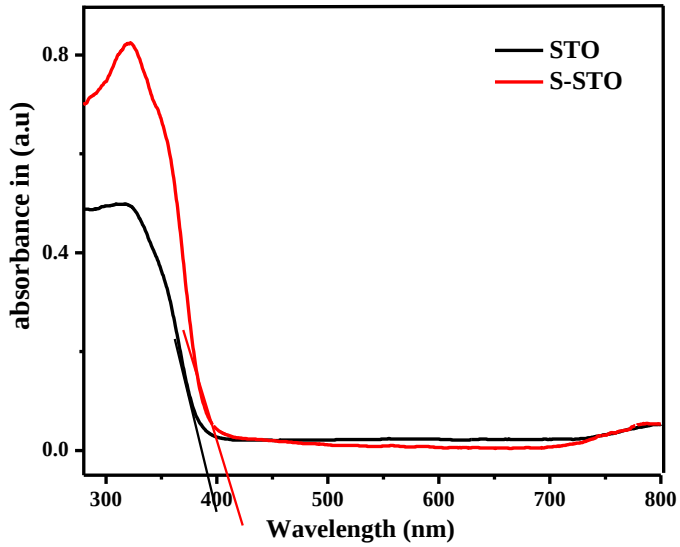

Fig 2. UV-vis absorption spectra of STO and S-STO.

Fig.2 shows absorption spectra of STO and S-STO samples. The absorption band of S-STO sample slightly shift towards the visible region due to the charge-transfer from the dopant induced localized electronic states. The possibility of S dopant as cation or anion in the STO lattice can be accounted in the following way: i) S^{6+} cations can create an donor electronic energy levels below the conduction band of STO, ii) The possibility of S entering as anion into the STO lattice by mixing of 2p orbitals of O^{2-} with 3p orbitals of S^{2-} can also lead to the formation of an acceptor level above the valence band of STO. It has also been reported in the literature that S^{6+} dopant ions creates a dopant electronic energy level around 0.38 eV above the VB of STO which facilitates the visible light absorption (*9*). The band gap energy values were calculated by using the formula $E_g = 1240/\lambda$, where λ is the wavelength of maximum absorption of the catalyst. The calculated bandgap values were found to be 3.17 eV and 3.0 eV for STO and S-STO corresponding to the wavelengths of 391 nm and 412 nm respectively. Absorption coefficient (α) values of STO and S-STO was calculated from the following formula $\alpha = 4 \pi k / \lambda$, were k is the absorption

index or absorbance value and λ is wavelength of maximum absorption. The absorption coefficient values were found to be 0.016 and 0.024 for STO and S-STO respectively (*10*).

2.3. FTIR studies.

The characteristics broad bands around 3100-3600 cm^{-1} and 1640 cm^{-1} are attributed to stretching and bending vibrations of hydroxyl groups and water molecule adsorbed on the surface of STO (inset of Fig. S1). The characteristic peaks around 447 cm^{-1} and 537 cm^{-1} corresponds to the bending and stretching vibrations of Ti-O in TiO_6 octahedron (Fig. S1) (*11*). Three new bands observed for S-STO sample at 1093, 1133 and 1213 cm^{-1} are ascribed to the characteristic υ_3 vibrational frequencies of sulphate ions (SO_4^{2-}) coordinated to the metal atom as a bidentate ligand through Ti-O-S bond (*12*). The two bands observed at 980 cm^{-1} (υ_1) and 1133 cm^{-1} can be assigned to symmetric and asymmetric stretching vibration of S-O bonds of sulphate functional group on the surface of S-STO. The peak at 1213 cm^{-1} corresponding to the stretching frequency of S=O bond. The bands corresponding to υ_2 (~450 cm^{-1}) and υ_4 (~600-700 cm^{-1}) could not be monitored in the present case since they overlap with the STO bands (*9*).

2.4. SEM analysis:

SEM images of STO and S-STO photocatalysts shows multi sphere morphology and sulphur incorporation has slightly modified the spheres with agglomeration. The particles size distribution of STO vary from 0 μm to 0.5 μm with average particle size of 0.072 μm and the standard deviation was found to be ~0.032. Particle size distribution of S-STO vary from 17 μm to 18 μm with average particle size of 18.04 μm and the standard deviation was found to be ~ 0.019 (Fig. 3).

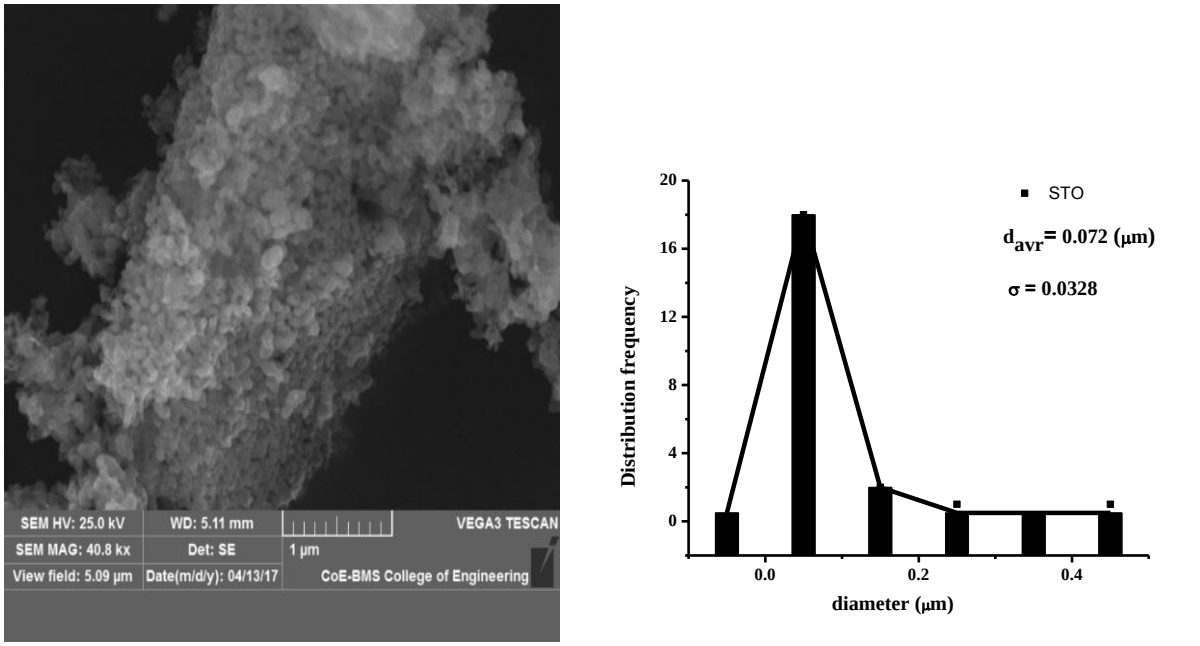

(A) STO

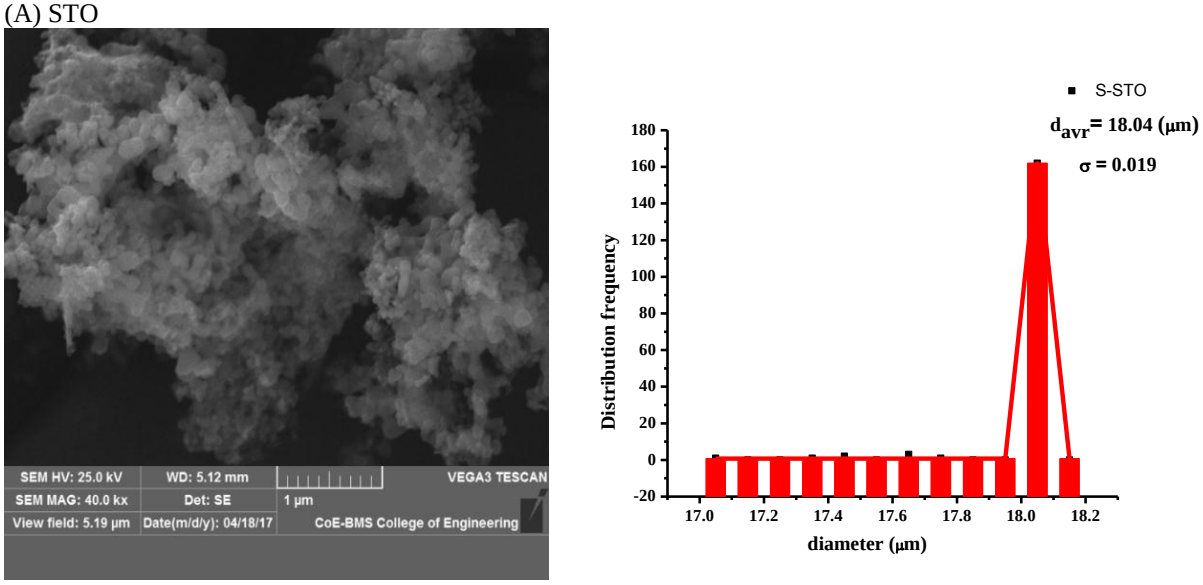

(B) S-STO

Fig. 3 SEM images, particles size distribution of (A) STO and (B) S-STO photocatalysts.

2.5. BET studies:

It is generally accepted that the efficiency of photocatalytic reactions is much dependent on the specific surface area and porosity of synthesized samples. Porous properties of the samples is investigated by Nitrogen adsorption and desorption isotherm measurements. The isotherms of the both the samples exhibit typically type-IV adsorption behavior with H3 hysteresis loops which is usually associated with aggregates of plate like particles giving rise to slit like pores, predominantly representing the mesoporous structure of the catalysts. The inset of Fig. S2 shows pore size distribution of the samples and they were analyzed from desorption branch of a nitrogen isotherm by the BJH method. The results indicated that S-STO sample has pronounced mesoporosity with smaller particle size and larger specific surface area when compared to STO. The specific surface area of the samples was found to be 23.61 m^2 g^{-1} and 14.22 m^2 g^{-1} for S-STO and STO respectively. The average pore diameter and the average pore volume was found to be 16.93 nm and 0.021 cm^3 g^{-1} and 12.53 nm and 0.074 cm^3 g^{-1} for S-STO and STO respectively.

2.7 XPS studies:

XPS measurements were used to investigate the chemical oxidation state of Sr, Ti, O and S elements in the prepared sample STO and S-STO. Fig. 4 (A) shows the high resolution spectra of Sr 3d peaks at binding energy (BE) values of 132.4 eV and 134.1 eV for STO and 132.07 eV and 133.9 eV for S-STO corresponding to the $3d_{5/2}$ and $3d_{3/2}$ spin state of strontium in Sr^{2+}. The Ti2p peaks observed at BE values of 458.7 eV and 464.7 eV for STO and 458.6 eV and 464.4 eV for S-STO are attributed to the $Ti2p_{3/2}$ and $Ti2p_{1/2}$ chemical states in which Ti is present in +4 oxidation state (Fig. 4 (B)). The observed small red shift of BE (~0.1 eV) for S-STO may be due to the different electronic interaction of Ti atom with less electronegative sulphur atom compared to oxygen atom. This interaction partially increases the electron density on Ti atom which in turn leads to the decrease of Ti2p BE value (*13*). The O1s BE peaks of STO is observed at 530 eV. The S-STO sample shows two O1s BE peaks at 530.52 and 533.04 eV indicating the presence of two kinds of oxygen. The BE peak observed at 530 and 530.5 eV can be due to the bulk lattice oxygen bonded to titanium for STO and S-STO respectively and the BE peak observed at 533.04 eV for S-STO can be assigned to the surface hydroxyl oxygen (Fig. 4 (C)). The BE peaks at 163.15 eV and 169.15 eV can be indexed to the presence of S dopant in two different oxidation states of S^{2-} and S^{6+} state (Fig. 4 (D)). (*14*).

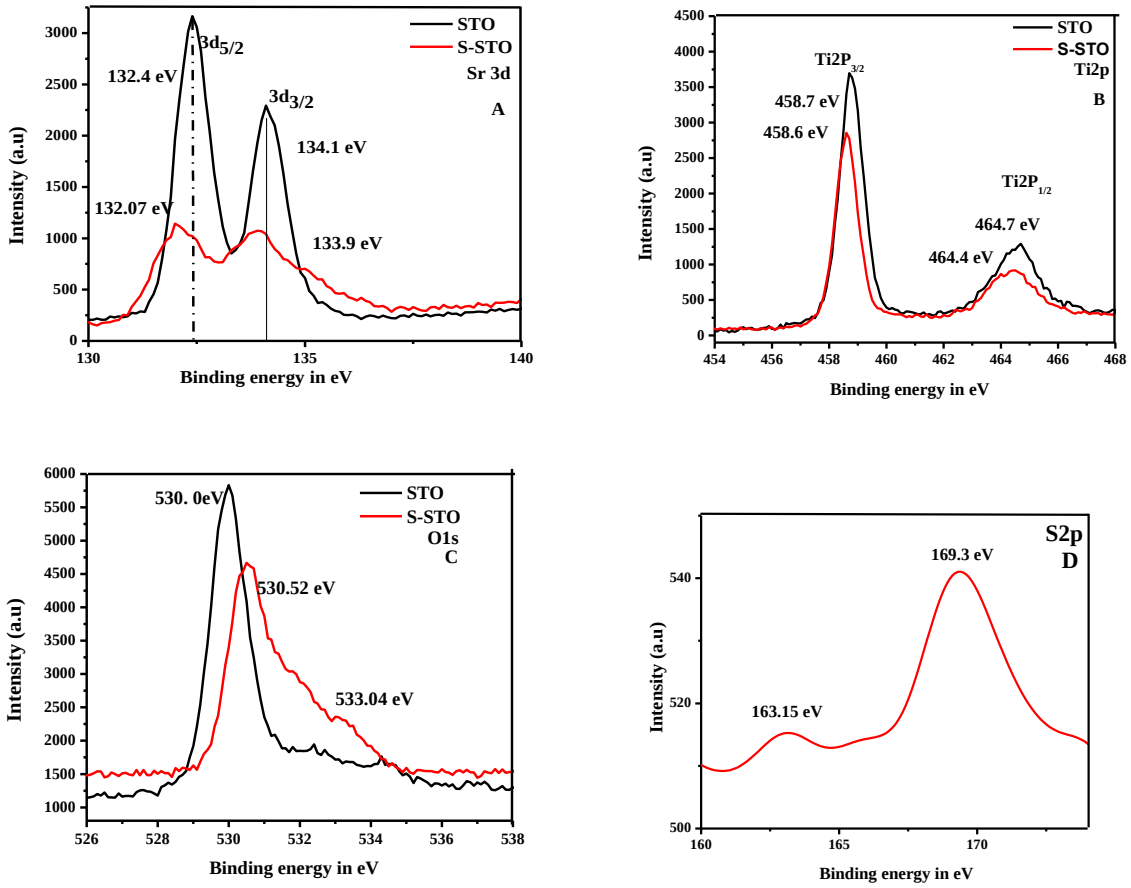

Fig. 4 High resolution XPS of (A) Sr3d, (B) Ti2p, (C) O1s and (D) S2p BE peaks of STO and S-STO samples.

2.6. Photoluminescence (PL) studies.

The PL is a multiphonon process and it is used to understand the separation and migration efficiency of photoinduced charge carriers. Thus this technique can be utilized to assess the presence of surface states, lifetime of the photoinduced charge carriers and fate of photogenerated electron-hole pairs in the semiconductor particles. PL emission originates from the

recombination of photoinduced electron hole pairs and thus the intensity of PL emission reflects the extent of rate of recombination. The PL emission around 420 to 440 nm is ascribed to the recombination process pertaining to band to band transitions from O 2p level to Ti 3d level. The observed emission at 440 nm is ascribed to the charge transfer transition from the central titanium to the neighboring oxygen anion within the TiO_6^{8-} octahedron (Fig. S3). PL intensities of this peak for S-STO is reduced by 45% when compared to STO sample. This decrease in PL intensity at 440 nm for S-STO sample can be due to the presence of sulphate ions (SO_4^{2-}) on the surface of sample which acts electron accepting centers. The presence of surface sulphate groups is substantiated by the FTIR technique. The peak at 475 nm is attributed to the presence of surface defects and also emission from the color centers associated with the oxygen vacancies (V_o). These neutral oxygen vacancies (V_o) can trap the excited electron giving rise to singly ionized oxygen vacancies with one electron ($V_o^{\cdot}$) located at ~ 0.82 eV below the CB and doubly ionized oxygen vacancies with two trapped electrons ($V_o^{\cdot\cdot}$) located ~ 0.51 eV below the CB (*15*).

2.7 Photoelectrochemical study.

2.7.1 Photocurrent measurements:

The transient photocurrent response test is an effective method to study the photoresponse of the semiconductor catalysts and the higher magnitude of the current is directly proportional to the charge separation and migration/transfer dynamics of photoinduced charge carriers. The efficiency of the photocatalyst is directly proportional to the difference in the magnitude of the dark current and the photocurrent. The higher the magnitude of photocurrent higher will be the efficiency of the photocatalyst. The photocurrent densities of S-STO (3.32×10^{-8} A) is higher than STO (1.0×10^{-8} A) indicating the generation of higher number of electron-hole pairs and their efficient separation (Fig. S4). The η current efficiency can be calculated by the following formula:

$$\eta = \frac{I_p - I_d}{qI_o} \qquad (2)$$

Where I_p and I_d are the current densities under illumination and in the dark respectively, I_o is the photon flux and q is the electronic charge. The calculated current efficiencies were found to be 2.36×10^{10} and 0.78×10^{10} for S-STO and STO respectively.

2.8. Photocatalytic activity.

Photocatalytic activities of STO and S-STO were evaluated for photodegradation of MV under solar light illumination (Fig. 5 (A)). It is well known that efficiency of photocatalysis depends on many factors such as charge carriers generation, separation, and migration, visible light absorption, diffusion path length and improved surface area of the photocatalyst. The photocatalytic activity of STO can be compared with the S-STO. 10% of MV was degraded in 120 min time period with STO as the catalyst and 99 % of MV was degraded with S-STO in 90 min time period (Fig. 5(B)).

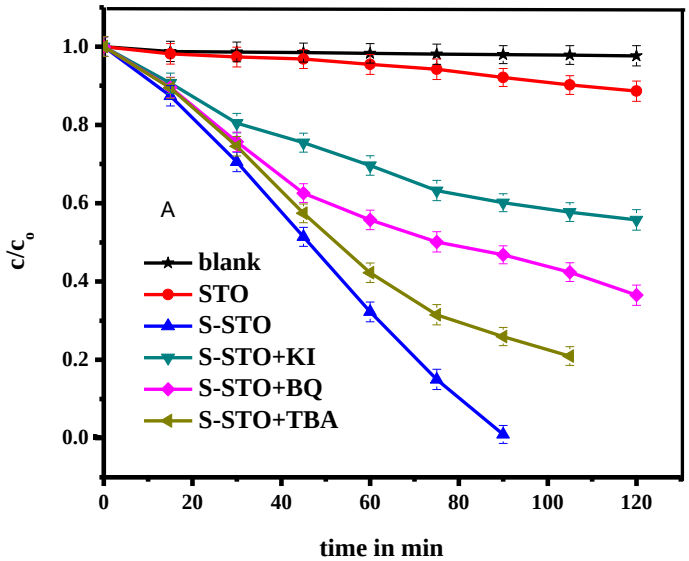

Fig. 5 (A) Plot of C/C_0 versus time for the degradation of MV under solar light illumination using STO and S-STO samples.

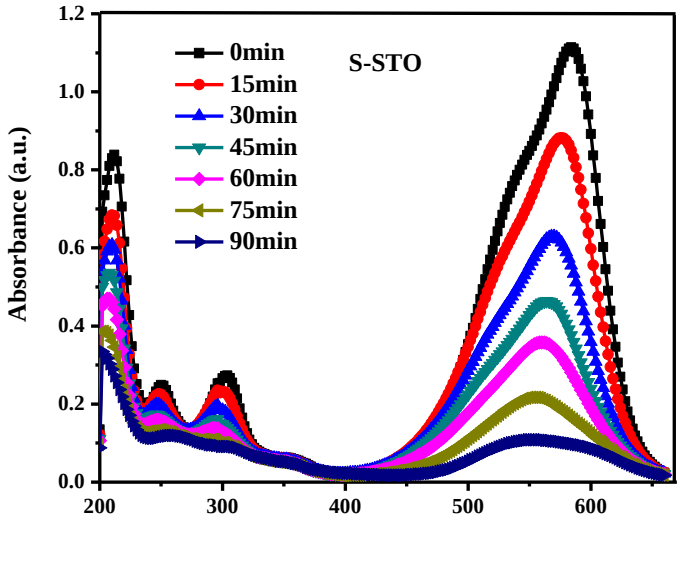

Fig. 5 (B) Degradation of MV using S-STO under solar light irradiation for 90 minutes.

The higher rate of photocatalytic activity of S-STO under visible light can be accounted in the following way: i) incorporation of S into the STO lattice in two different oxidation states of S^{6+} and S^{2-} creating donor and acceptor electronic energy levels within the host lattice will facilitate visible light absorption, ii) the incorporated S on the surface of the catalyst gets oxidized to SO_4^{2-} which acts as electron trapping center, iii) the trapped electron from SO_4^{2-} gets detrapped to the surface adsorbed oxygen molecules to produce superoxide radical(*16*), iv) the holes move to the surface of the catalyst to react with surface adsorbed hydroxyl anion to produce hydroxyl free radicals, v) surface SO_4^{2-} species acts as strong acidic sites, vi) the high electronegativity of S induces polarization of neighboring hydroxyl groups, vii) the highly polarized states along with higher surface acidity enhances the ability of trapping of photogenerated electrons, viii) the electrons are partially delocalized from oxygen to S in Ti-O-S bond making the an oxygen atom an electron deficient center which further prevents the recombination of photogenerated electrons, ix) S^{6+} ions possess empty s and p orbitals which can accommodate electrons in a shallow manner and it can detrap these electrons more efficiently either to the oxygen molecules or to the adsorbed pollutant molecules, x) lower crystallite size of S-STO decreases the migration path length of charge carriers, thereby enhances the availability of charge carriers in redox reactions, xi) higher surface area of S-STO facilitates higher extent of adsorption of substrate pollutant molecules, xii) synergistic effect between surface sulphate groups with the dopant S^{6+} enhances the rate of degradation and xiii) the electrical charge neutrality of S-STO is achieved by the creation of titanium vacancies V_{Ti} since, 2 S^{6+} ions can replace 3 Ti^{4+} ions (Scheme 1). In general the electronic structure of S-STO prolongs the life time of photogenerated charge carriers enhancing the degradation reaction rates. The photocatalytic activity of S-STO (k = 4.3564 × 10^{-2} min^{-1}) is 4.3 times higher than the STO (k = 0.01577× 10^{-2} min^{-1}).

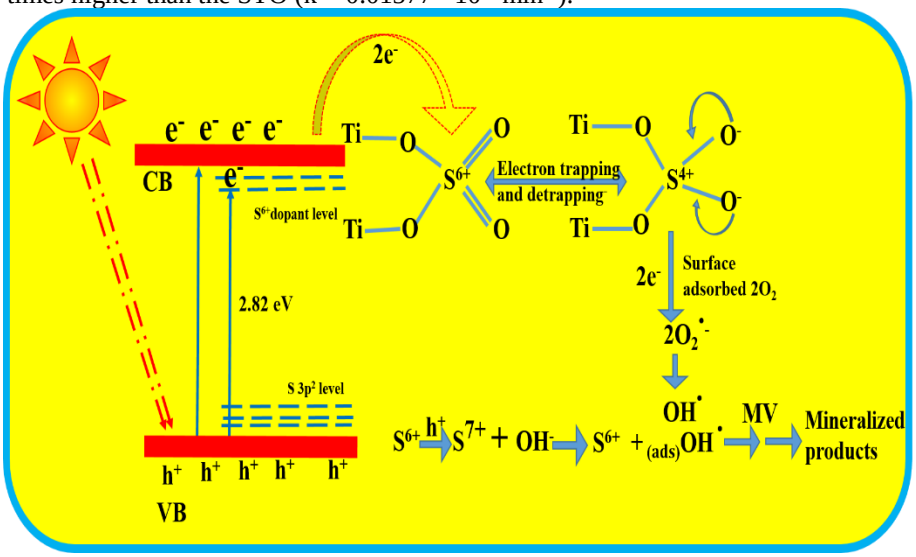

Scheme. 1 The mechanism of light absorption and electron hole separation in S-STO photocatalyst.

2.8.1 Photonic efficiency (ϕ_λ):

The photonic efficiency (ϕ_λ) was calculated by taking the ratio of rate of decomposition of MV (M_t) with respect to the total number of incident photons (L) in a given time t (*17*).

$$\phi_\lambda = \frac{M_t}{L} \qquad (3)$$

The rate of degradation (M_t) is given by the number of pollutant molecules decomposing in a given time t which is calculated by using the following formula:

$$M_t = \frac{4}{1000}.C_0 N.(1-e^{-kt}) \qquad (4)$$

Where, C_0 is the initial concentration of the pollutant, N is the Avogadro's number and k is first order reaction rate constant. The total number of incident photons in the given time period t is calculated by using the formula:

$$L = \frac{p\lambda t}{hc} \qquad (5)$$

Where p is the power of the light, λ is the wavelength, h is the Planck's constant and c is the velocity of light in the vacuum. Rate constant values, % degradation, photonic efficiency (ϕ_λ) and R^2 (linear regression coefficient) values are given in Table. S6.

3. Conclusions

The excellent photo catalytic activity of S-STO can be accounted to the synergistic effects between the doped electronic energy levels of S^{6+} ion with surface modified SO_4^{2-} ions. S-STO possess higher surface area, smaller crystallite size, higher light absorption coefficient, higher surface acidity, longer life time of charge carriers, extended absorption in the visible region and reduced band gap compared to STO. These better characteristics makes S-STO an excellent photocatalyst under solar light illumination.

4. Experimental Design

4.1. Chemicals

Tetra butyl titanate (97%) was obtained from Sigma Aldrich. Citric acid, strontium nitrate, ethanol (HPLC grade), sulphur powder were obtained from Merck Chemicals Limited. Ter-Butanol (TBA) and Benzoquinone (BQ) were obtained from Qualigens Fine Chemicals. Potassium iodide (KI) was obtained from SD Fine Chem Limited. Double distilled water was used throughout the experiment.

4.2 Preparation of photocatalysts

4.2.1. Preparation of catalyst.

STO was prepared by sol-gel method as reported earlier (*10*). S-STO was prepared by grinding calculated amount of STO (1 g) with a stoichiometric volume of sulphur solution (0.1 ml of 0.000262 g of sulphur prepared in 100 ml benzene) in a mortar and dried in an oven at 120 ^{0}C to get the desired dopant concentration of 0.15 at.%. The process of grinding is repeated for four to five times and the powder is finally calcined only at 200 ^{0}C for 5 h. Calcination temperature has to be maintained low since, the boiling point of sulphur is 445 ^{0}C. The optimum S dopant concentration is found to be 0.15 at. % from our previous research studies (*18*).

4.3. Characterization of the photocatalysts.

The powder X-ray diffraction (PXRD) patterns were obtained using Bruker D8 Advanced diffractometer, which was operated at 30 kV and 20 mA using Cu K α source with nickel filter at a scan rate of 2°/ minute. The X-ray diffraction line broadening data was obtained by reducing the scan rate to 0.5 °/ min. The Fourier transform infrared (FTIR) spectra were obtained using Bruker model Alpha–P IR spectrometer with diamond ATR cell. The absorption spectra were obtained using UV-vis spectrophotometer in the wavelength range of 200-800 nm (Schimadzu-UV 3101 PC UV-vis-NIR) with $BaSO_4$ as the reference standard. The absorbance data were used for the band gap measurement. The surface morphology was analyzed by scanning electron microscopic (SEM) technique using JSM840 microscope operating at 25 KV on specimen upon which a thin layer of platinum had been evaporated. The X-ray photoelectron spectroscopy (XPS) measurements were carried out using AXIS ULTRA from AXIS 165 integrated with Kratos patented Magnetic immersion lens along with charge neutralization system and spherical mirror analyzer. The spherical mirror analyzer provides real time chemical state and elemental imaging using the full range of pass energies and multi-point analysis from either real time or scanned images without the need for sample translation. All binding energies were calibrated to the C 1s peak at 284.8 eV of the surface adventitious carbon. The nitrogen adsorption–desorption isotherms were recorded using Nova Quanta Chrome Corporation 2006 Digisorb analyzer at liquid nitrogen temperature (77 K). The samples were degassed at 450°C prior to the measurement. The surface area was obtained by Brunner–Emmet–Teller (BET) method and pore size distribution was calculated from the Barret–Joyner–Halenda (BJH) model using adsorption isotherm. The photoluminescence (PL) data of the samples were measured using Cary Eclipse fluorescence spectrophotometer (Agilent technologies). Though the research work aims to use visible light irradiation for the study, experiments were also conducted under the illumination of UV light to understand the reaction mechanisms.

The photocurrent measurements were made using an electrochemical workstation (CH Instruments model CH601E) in a conv ential three electrode system. The electrochemical cell consists of platinum electrodes as anode and cathode (having an active surface area of ca. 0.5 cm^2) in an electrolyte (250 ml 0.1 M Na_2SO_4) suspension containing photocatalyst particles along with Ag/AgCl (saturated with 3 N KCl) as a reference electrode. The transient photocurrent responses of the pure and modified samples were investigated for several on and off cycles with a time interval of 20 seconds using a mercury vapour lamp (125

W) as a UV source. Photon flux of the UV light source (the wavelength of which is around 370 nm) was found to be 7.8 $mWcm^{-2}$ by ferrioxalate actinometry.

4.4. Photochemical reactor.

Experiments were carried out under direct sunlight between 11 a.m. to 2 p.m. during the summer season at Bangalore, India. The latitude and longitude are 12.58 N and 77.38 E, respectively using a circular glass reactor whose surface area is 176.6 cm^2. A typical experiment contains 100 mg of photocatalyst dispersed in 250 mL of 10 ppm Methyl violet (MV) solution. The reaction mixture was continuously stirred. The temperature of the reaction mixture was found to be around $28\text{-}30^0$ C. The average solar intensity was found to be 0.753 kW/m^2 (using solar radiometer). The intensity of the solar light was concentrated by using a convex lens and the reaction mixture was directly exposed to this concentrated sunlight. To compare the photocatalytic activity of the catalysts, experiments were simultaneously conducted to minimize the error arising due to the fluctuations in solar intensity. Aliquots of 5 ml were collected from the suspension at definite time intervals and was centrifuged to remove the catalyst particles for the spectrophotometric analysis. The residual concentration of the MV was determined by using UV-Vis spectrophotometer in the wavelength range from 200 - 800 nm, which shows a maximum at 584 nm. To determine the contribution of direct photolysis, a blank experiment was conducted by illuminating only the MV dye solution in the absence of photocatalyst.

Acknowledgements

Authors acknowledge the financial assistance from University Grants Commission (UGC), Department of Science and Technology (DST).

Conflict of interest:

There are no conflict of interest.

References

[1] J. Xu, Y. Wei, Y. Huang, J. Wang, X. Zheng, Z. Sun, L. Fan and J. Wu. "Solvothermal synthesis nitrogen doped SrTiO3 with high visible light photocatalytic activity." *Ceramics International* 40 (2014): 10583–10591.

[2] G. Wu, P. Li, D. Xu, B. Luo, Y. Hong, W. Shi, C. Liu. "Hydrothermal synthesis and visible-light-driven photocatalytic degradation for tetracycline of Mn-doped $SrTiO_3$ nanocubes." *Applied Surface Science* 333 (2015): 39–47.

[3] C. Zhang, Y. Jia, Y. Jing, Y. Yao, J. Ma, J. Sun. "Effect of non-metal elements (B, C, N, F, P, S) mono-doping as anions on electronic structure of $SrTiO_3$." *Computational Materials Science* 79 (2013): 69–74.

[4] K. Iwashina and A. Kudo. "Rh-Doped $SrTiO_3$ Photocatalyst Electrode Showing Cathodic Photocurrent for Water Splitting under Visible-Light Irradiation." *Journal of the American Chemical Society* 133 (2011): 13272–13275.

[5] J. Wang, S. Yin, M. Komatsu, Q. Zhang, F. Saito, T. Sato. "Photo-oxidation properties of nitrogen doped $SrTiO_3$ made by mechanical activation." *Applied Catalysis B: Environmental* 52 (2004): 11–21.

[6] J. Wang, S. Yin, Q. Zhang, F. Saito, T. Sato. "Synthesis and photocatalytic activity of fluorine doped $SrTiO_3$." *Journal of Materials Science* 39 (2004): 715– 717.

[7] P. Liu, J. Nisar, B. Pathak, R. Ahuja. "Hybrid density functional study on $SrTiO_3$ for visible light Photocatalysis." *International Journal of hydrogen energy* 37 (2012): 11611-11617.

[8] P. Periyat, C. P. Suresh, E. M. C. Declan, J. Colreavy, and J. H. Steven. "Improved High-Temperature Stability and Sun-Light-Driven Photocatalytic Activity of Sulphur-Doped Anatase TiO_2." *The Journal of Physical Chemistry C* 112 (2008): 7644–7652.

[9] G. Mishra, K. M. Parida, and S. K. Singh. "Facile Fabrication of S‑TiO_2/β-SiC Nanocomposite Photocatalyst for Hydrogen Evolution under Visible Light Irradiation" *ACS Sustainable Chemistry and Engineering* 3 (2015): 245−253.

[10] L. Gomathi Devi, B.G. Anitha. "Exploration of vectorial charge transfer mechanism in $TiO_2/SrTiO_3$ composite under UV light illumination for the degradation of 4-Nitrophenol: A comparative study with TiO_2 and $SrTiO_3$." *Surfaces and Interfaces* 11 (2018): 48–56

[11] N. G. Chandy, J.K. Thomas, R. Josec, H. Padma Kumar, M.K. Suresh, V. Ratheesh Kumar, P.R. Shobana Wariar , J. Koshy. "Synthesis and characterization of nanocrystalline strontium titanate through a modified combustion method and its sintering and dielectric properties." *Journal of Alloys and Compounds* 486 (2009): 711–715.

[12] B. Naik, K. M. Parida, and S. Chinnakonda, Gopinath. "Facile Synthesis of N- and S-Incorporated Nanocrystalline TiO_2 and Direct Solar-Light-Driven Photocatalytic Activity." *The Journal of Physical Chemistry C* 114 (2010): 19473–19482.

[13] J. Ni, S. Fu, C. Wu, J. Maier, Y. Yu, and L. Li. "Self-Supported Nanotube Arrays of Sulphur-Doped TiO_2 Enabling Ultrastable and Robust Sodium Storage." Advanced Materials 28 (2016): 2259–2265.

[14] C. Hana, M. Pelaez, V. Likodimos, A. G. Kontos, P. Falaras, K. O'Sheac, D. Dionysios. "Innovative visible light-activated sulphur doped TiO_2 films for water treatment." *Applied Catalysis B: Environmental* 107 (2011): 77– 87.

[15] C. Karuna karan and P. Gomathi sankar. "Solvothermal Synthesis of CeO_2−TiO_2 Nanocomposite for Visible Light Photocatalytic Detoxification of Cyanide." *ACS Sustainable Chemistry & Engineering* 1 (2013): 1555−1563.

[16] L. Gomathi Devi, M.L. ArunaKumari, B.G. Anitha, R. Shyamala, G. Poornima. "Photocatalytic evaluation of Hemin (chloro(protoporhyinato)iron(III)) anchored ZnO hetero-aggregate system under UV/solar light irradiation: A surface modification method." *Surfaces and Interfaces* 1–3 (2016): 52–58.

[17] D.S. Tsoukleris, A. I. Kontos, P. Aloupogiannis and P. Falaras, "Photocatalytic properties of screen-printed titania." *Catalysis today* 124 (2007): 110 – 117.

[18] L. Gomathi Devi, R. Kavitha. "Enhanced photocatalytic activity of sulphur doped TiO_2 for the decomposition of phenol: A new insight into the bulk and surface modification." *Materials Chemistry and Physics* 143 (2014): 1300-1308.

Electronic Supplementary material:

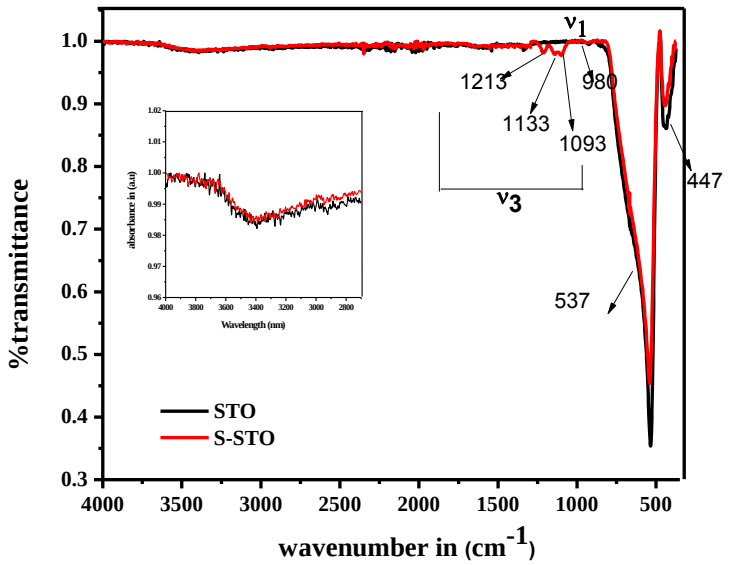

Fig. S1 FTIR spectra of STO and S-STO with the figure inset showing the bending vibrations of hydroxyl groups and water molecule.

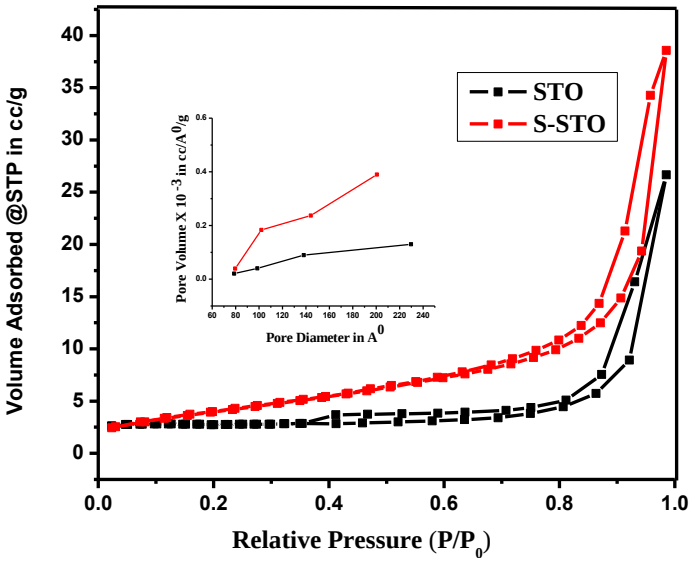

Fig. S2 Nitrogen adsorption-desorption isotherms of STO and S-STO and the inset of the figure shows the pore size distribution curve.

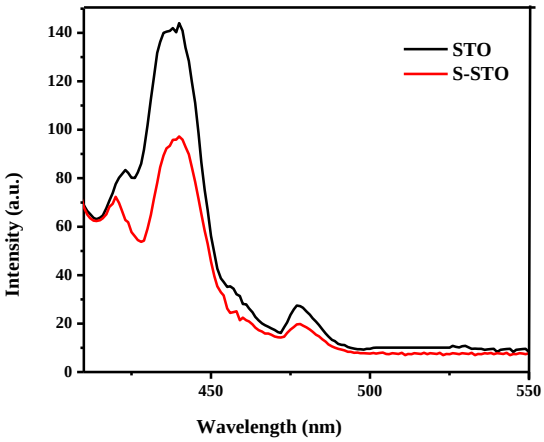

Fig. S3 PL spectra of STO and S-STO samples.

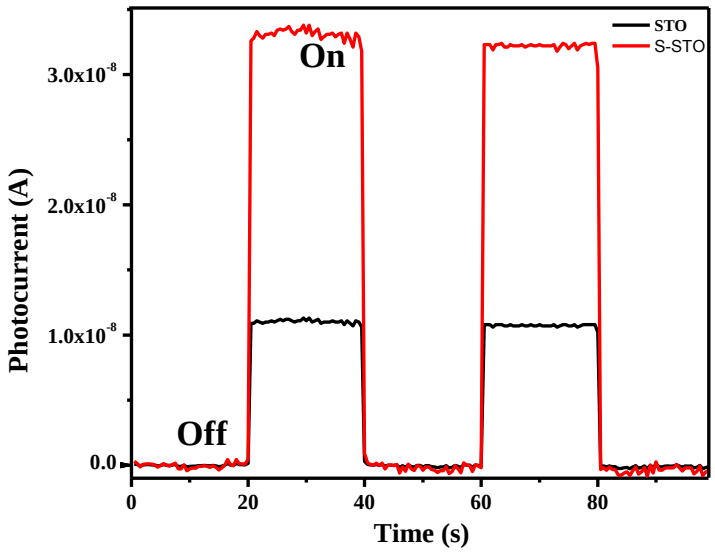

Fig. S4 Transient photocurrent responses of STO and S-STO.

Table S6 Rate constant values, % degradation and R^2 (linear regression coefficient).

Catalyst	% degradation	Time in min	Rate constant $k \times 10^{-2}$ min^{-1}	Photonic Efficiency $\phi_\lambda \times 10^{-11}$ mol L^{-1} m^2	R^2(linear regression coefficient)
MV	3	120	0.01577	0.321	0.9053
STO	10	120	0.0165	0.336	0.858
S-STO	99	90	4.3564	46.01	0.9985
S-STO+KI	50	120	0.4947	9.291	0.9725
S-STO+TBA	97	105	0.8284	14.72	0.9706
S-STO+BQ	80	120	3.396	40.85	0.9976